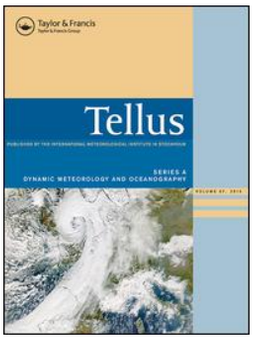

Tellus A: Dynamic Meteorology and Oceanography

ISSN: (Print) 1600-0870 (Online) Journal homepage: www.tandfonline.com/journals/zela20

Coupling of convection and circulation at various resolutions

Cathy Hohenegger, Linda Schlemmer & Levi Silvers

To cite this article: Cathy Hohenegger, Linda Schlemmer & Levi Silvers (2015) Coupling of convection and circulation at various resolutions, Tellus A: Dynamic Meteorology and Oceanography, 67:1, 26678, DOI: 10.3402/tellusa.v67.26678

To link to this article: https://doi.org/10.3402/tellusa.v67.26678

Tellus SERIES A DYNAMIC METEOROLOGY AND OCEANOGRAPHY
PUBLISHED BY THE INTERNATIONAL METEOROLOGICAL INSTITUTE IN STOCKHOLM

Coupling of convection and circulation at various resolutions

By CATHY HOHENEGGER*, LINDA SCHLEMMER and LEVI SILVERS,
Max Planck Institute for Meteorology, Hamburg, Germany

(Manuscript received 20 November 2014; in final form 17 February 2015)

ABSTRACT

A correct representation of the coupling between convection and circulation constitutes a prerequisite for a correct representation of precipitation at all scales. In this study, the coupling between convection and a sea breeze is investigated across three main resolutions: large-eddy resolution where convection is fully explicit, convection-permitting resolution where convection is partly explicit and coarse resolution where convection is parameterised. The considered models are the UCLA-LES, COSMO and ICON. Despite the use of prescribed surface fluxes, comparison of the simulations reveals that typical biases associated with a misrepresentation of convection at convection-permitting and coarser resolutions significantly alter the characteristics of the sea breeze. The coarse-resolution simulations integrated without convective parameterisation and the convection-permitting simulations simulate a too slow propagation of the breeze front as compared to the large-eddy simulations. From the various factors affecting the propagation, a delayed onset and intensification of cold pools primarily explains the differences. This is a direct consequence of a delayed development of convection when the grid spacing is coarsened. Scaling the time the sea breeze reaches the centre of the land patch by the time precipitation exceeds 2 mm day^{-1}, used as a measure for significant evaporation, yields a collapse of the simulations onto a simple linear relationship although subtle differences remain due to the use of different turbulence and microphysical schemes. Turning on the convection scheme significantly disrupts the propagation of the sea breeze due to a misrepresented timing (too early triggering) and magnitude (too strong precipitation evaporation in one of the tested convection schemes) of the convective processes.

Keywords: thermally induced mesoscale circulation, precipitation, sea breeze, convection-permitting, convective parameterisations, large-eddy simulations

1. Introduction

The distribution of convective precipitation, being at local, meso- or larger scales, is determined by the thermodynamical structure of the atmosphere and its interactions with dynamical processes. Although convective clouds can develop randomly as turbulent plumes rise through the boundary layer, their development is often linked to the existence of circulations. Such circulations can emerge from horizontal gradients in heating rates, either as a result of convection itself (e.g. Gill, 1980) or of external factors such as surface heterogeneity (e.g. Halley, 1753). The well-known tight interplay between convection and circulation is a critical factor hampering a correct representation of precipitation at all scales, but such scale interactions are difficult to assess (Slingo et al., 2003). The important role of circulation for understanding patterns of clouds and their response to climate change has been recently stressed by the formulation of a World Climate Research Programme (WCRP) Grand Challenge on Clouds, Circulation and Climate sensitivity (Bony et al., 2015).

The situation of a sea breeze interacting with convection is a natural laboratory to investigate issues related to convection–circulation coupling and their representation across resolutions. Sea breezes affect the precipitation distribution over many regions of the Earth (Yang and Slingo, 2001; Sato et al., 2009). On the one hand and as compared to a situation without a background pre-existing circulation, sea breezes alter the timing, amount and location of precipitation (e.g. Pielke, 1974; Burpe and Lahiff, 1983; Lynn et al., 1998). On the other hand, the development of clouds and precipitation modifies the sea breeze characteristics (Berg and Oerlemans, 1985; Segal et al., 1986; Nicholls et al., 1991) and especially leads to a faster propagation of

*Corresponding author.
email: cathy.hohenegger@mpimet.mpg.de

Citation: Tellus A 2015, **67**, 26678, http://dx.doi.org/10.3402/tellusa.v67.26678

the breeze front (Rieck et al., 2015). Besides such effects, the evolution of a sea breeze is also strongly controlled by factors such as coastline curvature, background wind, stability or surface fluxes (see Crosman and Horel, 2010, for a review).

Numerous studies have assessed the ability of a specific model to capture the precipitation characteristics in coastal or island regions and have highlighted the dependency of the results on parameterisation choices (e.g. Lynn et al., 2001; Cohen, 2002; Lynn and Khain, 2007; Kuell and Bott, 2008). Although numerous, such studies have tended to focus on one specific resolution as well as on the triggering of convection and resulting precipitation characteristics rather than on the coupling between convection and the sea breeze. Aspects of the coupling between convection and sea breeze-like circulations across different model configurations have been recently investigated in Langhans et al. (2013) for orographic convection, in the CASCADE project for the African monsoon system (Garcia-Carreras et al., 2013; Marsham et al., 2013) and for a situation of convection triggered by soil moisture-induced circulations (Taylor et al., 2013). The latter studies made use of comparison among simulations performed at different convection-permitting resolutions [grid spacing of O(1–12) km] with and without a convection scheme. They revealed that convection schemes have difficulties in reproducing such coupled systems. Langhans et al. (2013) noted that the too early development of cloud cover due to the use of a convective parameterisation induces a weakening of the convergence associated with the plain-mountain circulation, whereas the CASCADE project emphasised both the too early triggering of convection and the absence of cold pools in convective parameterisations as causes for a misrepresented monsoon. Even though the benefits of convection-permitting simulations over parameterised convection have been documented in various contexts (Kain et al., 2006; Hohenegger et al., 2008; Sato et al., 2009; Prein et al., 2013), the former simulations also suffer from typical biases, for instance a too late triggering of convection (Petch et al., 2006; Lean et al., 2008; Baldauf et al., 2011).

The goal of this study is to systematically investigate the coupling between convection and a sea breeze across a range of resolutions. The resolutions considered are large-eddy resolution where convection is fully explicit, convection-permitting resolution where convection is partly explicit and coarse resolution where convection is parameterised. A special emphasis is on biases in the representation of the sea breeze characteristics that originate from a poor representation of convection at convection-permitting and coarser resolutions. The specific role of misrepresented convection characteristics such as timing, cold pools or heating profiles will be quantified and the main reason for the documented biases isolated.

The outline of the paper is as follows. Section 2 describes the method and gives specific information on the chosen models as well as on the case and experimental set-up. Section 3 presents the main simulation characteristics with an emphasis on precipitation and associated sea breeze characteristics. The differences observed in section 3 among the various simulations are explained in section 4, first in light of a misrepresentation of physical processes and second with respect to parameterisation choices and model design. The generality of the results is investigated in section 5 and conclusions are given in section 6.

2. Method

2.1. Models

We consider three different atmospheric models which have been designed to work in specific resolution ranges. The models considered are the University of California Los Angeles Large-Eddy Simulation model UCLA-LES (see Stevens et al., 2005), the COnsortium for Small-scale MOdeling model COSMO (see Baldauf et al., 2011) and the ICOsahedral Non-hydrostatic model ICON (see Zängl et al., 2014). The UCLA-LES model assumes that the largest eddies of the flow are explicitly resolved and is run at sub-kilometer grid spacing. The UCLA-LES has been frequently applied to study small-scale processes such as boundary layer, cloud and convection including their interactions with the land surface (e.g. Siebesma et al., 2003; Ackerman et al., 2009; Rieck et al., 2014). The COSMO and ICON models cover convection-permitting resolution as well as coarser resolution with parameterised convection. The COSMO model is run operationally with a grid spacing of 2.2 and 6.6 km at MeteoSwiss or of 2.8 and 7 km at the Deutscher Wetterdienst (DWD), the coarser mesh sizes of 6.6 and 7 km using parameterised deep convection. The ICON model replaced the global model GME of DWD in January 2015 and will replace the 7-km version of the limited-area model COSMO in late 2015. The physical parameterisations of the three models are briefly described in the following. Given the case and experimental set-up (see sections 2.2 and 2.3) the parameterisations of relevance are boundary layer, microphysics and convection. Radiation is turned off in all the simulations.

The UCLA-LES solves the three-dimensional anelastic equations of motion based on centred differencing and third-order Runge-Kutta time integration. Subgrid-scale turbulent processes are parameterised after Smagorinsky. The microphysics scheme is the two-moment scheme of Seifert and Beheng (2006). The scheme predicts the evolution of cloud water, rain, hail, graupel, snow and ice.

The COSMO model solves the fully three-dimensional non-hydrostatic and compressible Navier Stokes equations.

The employed version of the model corresponds to version 4.19.3. The time integration is performed by a third-order Runge-Kutta scheme with time splitting between fast and slow modes. Boundary layer processes are parameterised using a prognostic turbulent kinetic energy closure at level 2.5 based on Mellor and Yamada (1982) including effects from subgrid-scale condensation and from thermal circulations (Raschendorfer, 2001). Microphysics is parameterised as a one-moment cloud microphysics scheme including cloud water, rain, snow and ice (Doms et al., 2011) with the addition of graupel as a third ice category (Reinhardt and Seifert, 2006). Finally, the mass-flux convection scheme of Tiedtke (1989) is used. The scheme handles shallow, deep and mid-level convection.

The ICON model shares some similarities with the COSMO model but also exhibits some very distinct characteristics, especially in terms of grid discretisation and chosen convection scheme. The ICON model (revision number 16400) solves the fully three-dimensional non-hydrostatic and compressible Navier Stokes equations. The base grid cells of ICON are triangles. ICON uses an icosahedral–triangular C grid and a combination of first and second order finite difference spatial discretisation (Wan et al., 2013). The integration in time consists of a two-time level predictor corrector scheme with the physics parameterisations split into slow and fast modes. As in COSMO, the boundary layer scheme of Raschendorfer (2001) is used whereas for the microphysics, graupel is not considered. The convection scheme stems from the European Centre for Medium-Range Weather Forecasts (ECMWF) Integrated Forecast System (IFS) model. It is based on the Tiedtke (1989) scheme with subsequent modifications by P. Bechtold (Bechtold et al., 2008). A comprehensive description of the convection scheme can be found in the IFS documentation (available at http://old.ecmwf.int/research/ifsdocs/CY38r1/IFSPart4.pdf).

2.2. *Initial and boundary conditions*

A prototype case is designed to mimic the situation of a sea breeze interacting with precipitating convection, which serves as an archetype for a case of convection interacting with a thermally induced circulation. The case is loosely based on observations taken on the North Sea coast during summer, a region that experiences land–sea breezes. Sensitivity to the chosen case set-up, specifically initial profile, surface fluxes and domain size, is investigated in section 5.

The case set-up requires defining an initial profile of temperature, humidity and wind to start the simulations, as well as prescribing values at the bottom boundary conditions. To define the initial profile soundings taken at Norderney (53.4° N; 7.08° E), a small island right off the North Sea coast of Germany, are used. Only convective days, defined as days with a CAPE value larger than 250 J kg^{-1} at 12 Z, are retained. The resulting profiles of temperature and specific humidity are averaged over one summer month (July 2012) and displayed in Fig. 1a and 1b. To make it easier to control specific aspects of the profiles, the observed profiles are idealised. For the temperature a linear decrease in temperature with a slope of 6.6 K per km up to 9 km and a slope of 1 K per km higher up is chosen. As can be seen in Fig. 1a, the idealised profile captures well the observed temperature gradient in the troposphere and lower stratosphere, although the inversion near the tropopause cannot be reproduced per construction. The temperature at the ground amounts to 17.3°C. A second idealised temperature profile is defined in Fig. 1a by the blue curve. This second profile typifies the situation of a very stable atmosphere with a temperature decrease of 5.5 K per km up to 9 km. It will be used in section 5 to assess the generality of the results.

For the specific humidity, instead of directly fitting a curve to the observed specific humidity, the relative humidity

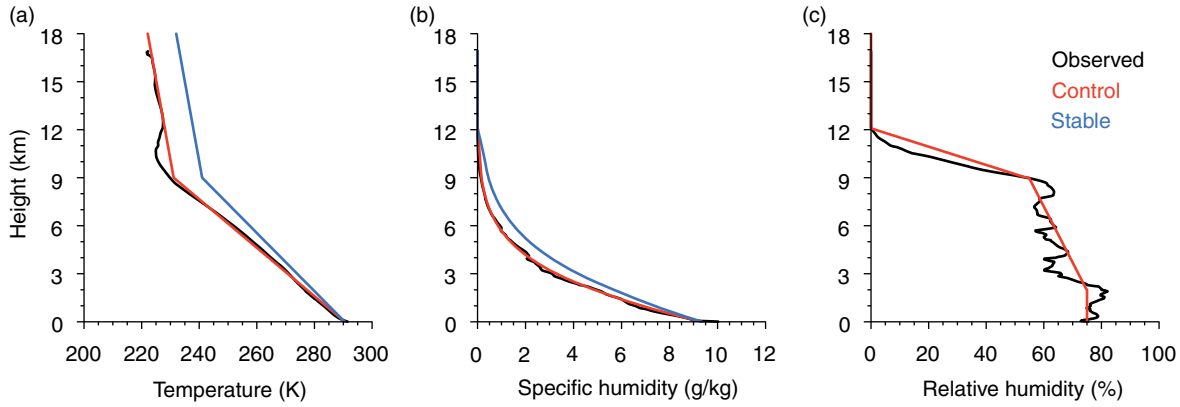

Fig. 1. Profiles of (a) temperature (K), (b) specific humidity (g kg^{-1}) and (c) relative humidity (%) derived from soundings taken at Norderney (black, see text for details) and as idealised to start the model simulations (red, control). The stable case (blue) uses a more stable temperature profile but the same relative humidity as the control.

is computed, fitted and then converted back to specific humidity (see Fig. 1b and 1c). The relative humidity is assumed constant in the lower 2 km with a value at 75%. The relative humidity then decreases by 20% between 2 and 9 km and by 17.5% per km higher up. Although more complicated this procedure gives better agreement with the observed specific humidity profile than, for instance, prescribing an exponentially decaying specific humidity. The same relative humidity profile is employed for the control and stable cases yielding higher specific humidity values in the stable case. The winds are set to zero.

At the bottom boundary free slip as well as fixed fluxes of sensible and latent heat are used. The surface fluxes take two different values on the left part (ocean) and right part (land) of the domain (see Fig. 2) in order to generate a sea breeze. As the domain is periodic in horizontal directions, Fig. 2 actually mimics the situation of an infinitely elongated peninsula. Sea breezes are triggered at the two coastlines (at 0 and 409.6 km) and propagate inland until colliding in the middle of the land stripe (see section 3). Over ocean, the sensible heat flux is set to 0 W m^{-2} and the latent heat flux to 50 W m^{-2}. The corresponding land values are 120 W m^{-2} and 150 W m^{-2}. These values are similar to monthly averages of surface fluxes as simulated by the operational COSMO model across the North Sea coast during summer. The use of prescribed fluxes ensures that the buoyancy difference between land and ocean, which is a known factor influencing the propagation speed of a sea breeze (Benjamin, 1968; Rotunno, 1983; Robinson et al., 2013), remains the same across the simulations. Also, for this initial analysis, only the case of stationary surface fluxes is considered.

2.3. *Experimental set-up*

The domain (see Fig. 2) spans 819.2 km by 404 km and is periodic in the two horizontal directions. The domain is large enough both in x- and y-directions to allow several convective cells to develop. The chosen domain size is a compromise between the number of points that need to be present at low resolution and the number of points that can be simulated at very high resolution. Repeating the high-resolution simulations on a smaller domain revealed an identical sea breeze propagation indicating that the simulations are not affected by boundary effects and that the chosen domain is indeed large enough.

The large-eddy simulations performed with the UCLA-LES model employ a horizontal grid spacing of 400 m and a vertical spacing of 100 m below 1 km stretching to more than 500 m in the upper layers with a total of 88 vertical layers. The model top lies at 24 km with a Raleigh damping layer damping vertically propagating waves above 18 km. The model physics is as described in section 2.1. The simulations are referred to as UCLA04, UCLA standing for UCLA-LES and 04 for the employed grid spacing (namely 0.4 km). A grid spacing of 400 m allows an explicit representation of deep convection but could misrepresent smaller-scale phenomena including the transition to deep convection. This seems not to be an issue in the present case where the use of an unstable profile and the existence of a sea breeze concur to a rapid and strongly controlled development of convection (see section 3). As such UCLA04 serves as our reference case. Sensitivity to the chosen grid spacing is actually explored in section 4.2.

The convection-permitting simulations are integrated with the COSMO model with a grid spacing of 0.02° (2.2 km). The model top sits at 22 km. There are 88 stretched vertical levels, whereby 10 levels are distributed in the first 1000 m. A sponge layer is used starting at 18 km. The physics parameterisations are described in section 2.1, but the convection scheme is turned off. Shallow convection is also turned off. The simulations are referred to as COSMO2 with 2 as a short for the chosen grid spacing of 2.2 km. Sensitivity of the results to parameterisation choices, especially microphysics, turbulence and shallow convection is investigated in section 4.2.

Finally the COSMO and ICON models are used to conduct the coarser-resolution simulations with parameterised

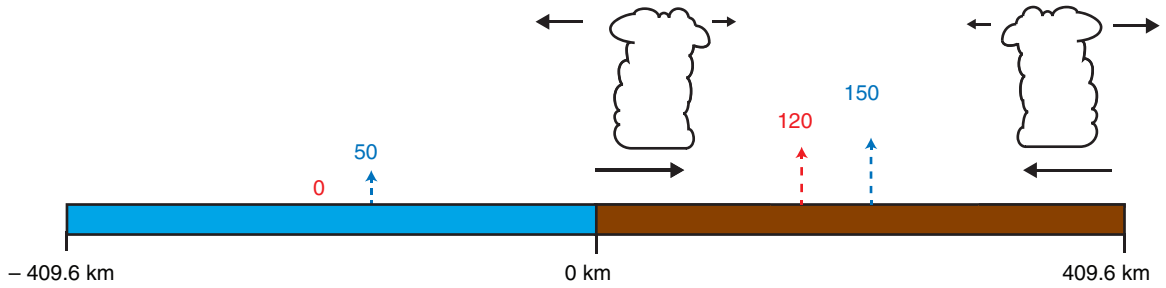

Fig. 2. Overview of the simulation set-up with domain size in x-direction, values of sensible (red) and latent heat fluxes (blue; in W m^{-2}) over ocean (left) and land (right) as well as schematic of the horizontal component of the circulation and cloud location. Note that the domain is doubly periodic.

convection. The COSMO model is run at 0.1° (11 km) and the corresponding experiment is called COSMO11p. The suffix p makes clear that the convective parameterisation is turned on. Except for the grid spacing, a longer time step (100 s instead of 20 s) and the switching on of the convection scheme (both shallow and deep), the model set-up is akin to the one in COSMO2. The ICON model is integrated using triangles with an area of 92.16 km^2 and a distance between the centre of the triangles of 8.5 km. The model top lies at 25 km with 100 vertical levels and a Rayleigh damping of vertically propagating waves. The ICON simulations are named ICON8p. Both the COSMO11p and ICON8p simulations are repeated with the convection scheme turned off. The latter simulations are called COSMO11 and ICON8.

It is to note that the boundary between land and ocean in ICON does not follow a straight line as with the UCLA-LES or with the COSMO model but takes on a zigzag pattern following the triangles' edges. This is similar to what will happen over certain regions in global simulations performed with ICON.

3. Precipitation and sea breeze characteristics

The main simulation characteristics in terms of precipitation and circulation patterns are described in this section. The analysis is restricted from simulation start to 2 h after the opposing breeze fronts have collided in the centre of the land patch. Two hours are chosen so as to include the precipitation event associated with the collision of the breeze front.

Figure 3 shows time series of precipitation and cloud top height for the various experiments. All the simulations support the formation of deep convective clouds that rapidly precipitate, but differences exist. Comparing the various curves, the simulations seem to primarily cluster according to their treatment of convection rather than to the chosen model. All the simulations without convective parameterisation (UCLA04, COSMO2, COSMO11 and ICON8) reproduce one main precipitation event with two precipitation maxima. The first maximum, after 10.5 h in UCLA04, 11 h in COSMO2, 14 h in ICON8 and 15 h in COSMO11, is associated with the gradual development of convective cells and generally occurs 2–3 h after the clouds have reached their maximum depth (compare Fig. 3a and 3b). This first maximum becomes less pronounced with increasing resolution. The second precipitation maximum results from the collision of the opposing breeze fronts in the centre of the land patch. Despite a similar overall behaviour, the simulations differ in terms of timing and precipitation amounts. The fact that precipitation amounts can widely differ despite the use of a very constrained simulation set-up, especially between UCLA04 and the remaining

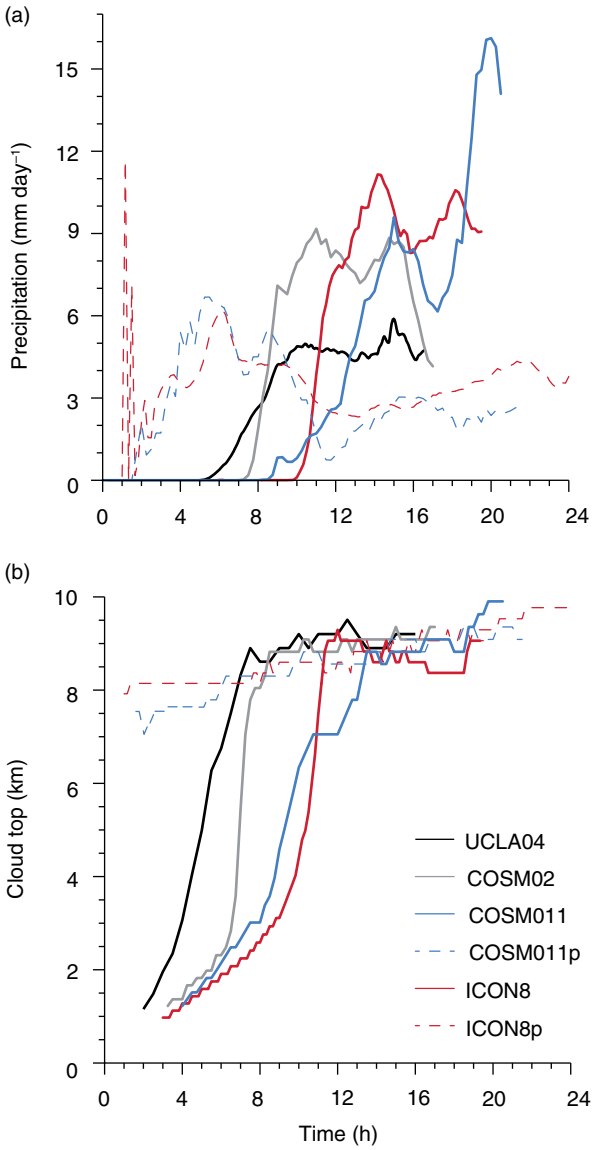

Fig. 3. Time series of (a) domain-averaged precipitation (mm day^{-1}) and (b) maximum cloud top height (km) in UCLA04 (black), COSMO2 (grey), COSMO11 (blue) and ICON8 (red). Dashed lines for the simulations with convective parameterisation.

simulations, is not surprising given the use of very different microphysics schemes (e.g. Van Zanten et al., 2011).

The two experiments using convective parameterisation (COSMO11p and ICON8p) in contrast display two distinct precipitation events, one from 1 to 12 h and one from 12 to 24 h. Various local maxima exist. These two events are associated with very distinct circulation characteristics (see below). The collision of the breeze fronts, which occurs after 19.25 h in COSMO11p and 21.75 h in ICON8p (see Table 1), also does not lead here to a sharp increase in precipitation as was the case with the experiments integrated without convective parameterisation.

Biases associated with the representation of convection that are known from realistic configurations remain present in our idealised set-up and can be clearly recognised in Fig. 3. COSMO11p and ICON8p trigger convection too early in the day, a well-known problem of convective parameterisations (e.g. Yang and Slingo, 2001; Dai, 2006; Brockhaus et al., 2008). In contrast the onset of convection is delayed in COSMO2 as compared to UCLA04. Once triggered the deepening of convection is nevertheless faster in COSMO2 than in UCLA04. Similar biases have been documented in real-case convection-permitting simulations performed with COSMO (e.g. Baldauf et al., 2011; Kühlein et al., 2014). Such biases are thought to be associated with an actually too coarse grid spacing for an explicit representation of convection. Especially the missing small-scale variability, the need to saturate a larger grid box and weaker lateral entrainment all contribute to a delayed but more rapid deepening of convection at convection-permitting resolutions. Removing the convective parameterisation as in COSMO11 and ICON8 gives a precipitation time series more akin to COSMO2. Similar results have been obtained in various real-case applications (e.g. Hohenegger et al., 2008; Pearson et al., 2014). As expected, the triggering of convective cells and hence the production of precipitation is even more delayed in COSMO11 or ICON8 as compared to UCLA04.

An overview of the circulation and associated cloud pattern is given in Fig. 4. In agreement with Fig. 3, UCLA04, COSMO2, COSMO11 and ICON8 all display a similar pattern. The latter is characterised by a sharp front and an organisation of the clouds at the breeze front. The shallow return current associated with the inland propagation of the sea breeze, generally located at the top of the boundary layer in a dry atmosphere (e.g. Antonelli and Rotunno, 2007), has merged with the cloud circulation and the outflow current at the top of the clouds. These various characteristics are as expected for a case of convection interacting with a sea breeze (e.g. Pielke, 1974). Although differences in timing exist, this pattern emerges in the four simulations once deep convective clouds have formed.

The simulations with parameterised convection COSMO11p and ICON8p show a qualitatively different behaviour. The morning circulation associated with the first precipitation event (Fig. 4e and 4f) does not exhibit the characteristics of a typical sea breeze. There are also differences between COSMO11p and ICON8p with a circulation concentrated in the middle rather than lower levels in ICON8p. This reflects differences in the cloud population. As can be recognised from the vertical location of grid-scale clouds in Fig. 4e and 4f COSMO11p supports deep clouds that only detrain slightly above 6 km. In contrast ICON8p produces a larger variety of convective clouds with clouds detraining between 6 and 8 km, 2 and 4 km as well as around 1 km. Differences in the entrainment formulation between the COSMO and ICON convection schemes, especially a stronger sensitivity to relative humidity in ICON (see Bechtold et al., 2008), may explain such differences (see also De Rooy et al., 2013; Derbyshire et al., 2004).

The circulation and cloud patterns in COSMO11p and ICON8p become more similar to each other, to the remaining simulations and to the archetype case of a sea breeze interacting with convection during the second precipitation event (Fig. 4g and 4h). A shallow low-level circulation exists with a clear front and an enhancement of the cloud cover towards the breeze front. The features tend nevertheless to be less sharp than in Fig. 4a–4d, and the return current has not merged with the outflow current at the top of the clouds.

To get a better sense of the evolving circulation characteristics and their differences among the simulations, Fig. 5 shows a time series of the breeze front location. The location of the breeze front is defined as the location, measured from $x = 0$ km (see Fig. 2), where the u component of the wind velocity drops below 1 m s^{-1} in the lowest model layer. Using a smaller threshold yields noisier curves with a faster propagation of the breeze front but does not affect the inherent differences among the various simulations. Using other proxies to define the location of the breeze front, like horizontal pressure gradient or horizontal temperature gradient, also leads to similar differences among the various simulations. This is because, as in the case of a sea breeze propagating in a dry atmosphere, the buoyancy difference between the two fluids causes a pressure and hence a wind response (see also section 4.1). For the computation of the location of the breeze front, u is first averaged in y-direction. Figure 5 also entails dots that mark the time the two opposing breeze fronts, one propagating from $x = 0$ km towards the centre of the land patch and one

Table 1. Summary of various quantities associated with the propagation of the breeze front in the experiments: T_{col} (h), T_{acc} (h) and V (m s^{-1}). The values in brackets refer to the first precipitation event in COSMO11p

	UCLA04	COSMO2	COSMO11	ICON8	COSMO11p	ICON8p
T_{col}	14.5	15	18.5	17.5	19.25 (8.75)	21.75
T_{acc}	8.5	9.5	13.5	12.5	15 (4)	14
V	7.5	8.6	6.8	7.1	13.8 (13.2)	7.6

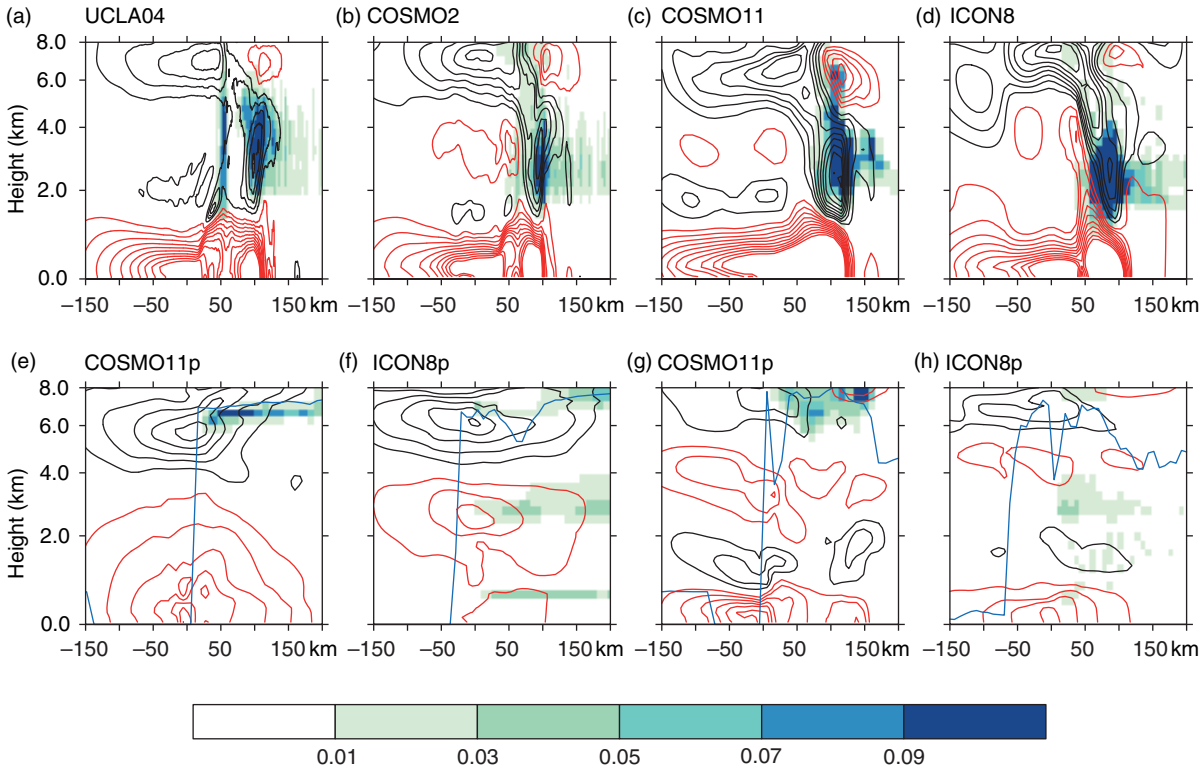

Fig. 4. Vertical cross sections (y-averaged) of resolved cloud water and cloud ice (shaded, g kg^{-1}) and u wind velocity (contour lines each 0.5 m s^{-1}, red positive, black negative) at time of maximum precipitation for the simulations with explicit convection: (a) UCLA04 (10.5 h), (b) COSMO2 (11 h), (c) COSMO11 (15 h), (d) ICON8 (14 h). Panels (e–h) are for the simulations with parameterised convection after (e, f) 6 and (g, h) 16.5 simulation hours. The blue line on (e–h) denotes the convective cloud top.

from $x = 409.6$ km (see Fig. 2), collide or, equivalently, reach the centre of the land patch. This collision time is denoted by T_{col}. Since the breeze fronts do not necessarily collide or reach the centre of the land patch especially at coarser resolution due to the coarser grid spacing, T_{col} is computed as the time the breeze front reaches its farthest inland extent. If the breeze front stays stationary for some time before retracting back towards the coast, T_{col} corresponds to the averaged times.

The simulations in Fig. 5 seem again to first cluster according to their treatment of convection, being explicit or parameterised. The two simulations with parameterised convection (COSMO11p and ICON8p) exhibit two breeze events, one before and one after 12 h. The first event is particularly visible in COSMO11p: the breeze front rapidly propagates inland between 4 and 8 h covering a distance of 180 km before retracting back to the coast. The remaining simulations display only one breeze event. The curves lie on top of each other during the first 5 h before diverging. The collision (see also Table 1) occurs first in UCLA04 followed by COSMO2, ICON8 and finally COSMO11. The differences in T_{col} as compared to UCLA04 range from 0.5 h (COSMO2), 3 h (ICON8) to 4 h (COSMO11).

Both the behaviour of COSMO11p and ICON8p with two breeze events as well as the differences in T_{col} among the simulations with explicit convection are reminiscent of the overall differences in the development of convection displayed by Fig. 3. It follows that misrepresentations of convection at convection-permitting or coarser resolution are strong enough to project onto the sea breeze characteristics despite the use of fixed surface fluxes. Recall that the propagation speed of a sea breeze primarily depends upon the buoyancy difference between land and ocean in a dry atmosphere (Benjamin, 1968; Rotunno, 1983; Robinson et al., 2013) and that the only difference between COSMO11 and COSMO11p as well as between ICON8 and ICON8p is the switch to the convection scheme. The results are consistent with Rieck et al. (2015) who, based on an analysis of fully coupled large-eddy simulations over an heterogeneous surface, showed that the formation of clouds and precipitation modifies the propagation of the breeze front (see section 4.1).

To further check the causal relationship between biases in convection and biases in the sea breeze characteristics as both entities strongly interact, all the simulations are repeated in a dry modus. This is achieved by setting the

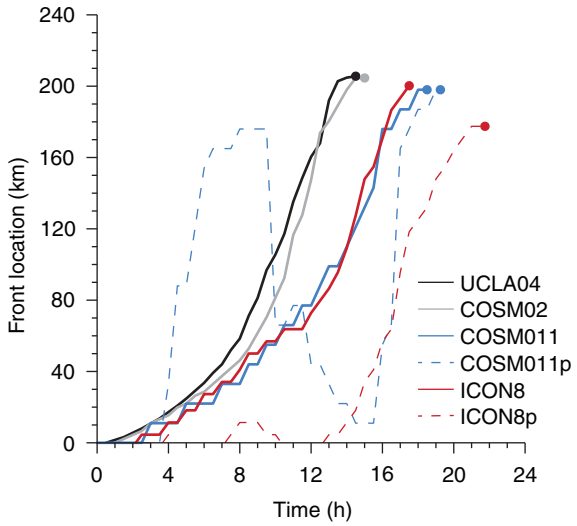

Fig. 5. Time series of the location of the breeze front (km), measured from the coastline $x = 0$ km, until the breeze front collides (dots) in the various experiments. Line style as in Fig. 3.

latent heat flux and the specific humidity to zero. In that case (not shown) COSMO2 begins to diverge from UCLA04 after 10 h and exhibits a faster propagation. COSMO11 is able to keep track of UCLA04, whereas ICON8 begins to lag behind UCLA04 after 16 h. Hence the simulations begin to diverge from each other at a later time in the dry than in the wet case. Furthermore they reveal a different ordering of the collision times, confirming that biases in convection primarily cause the documented circulation biases.

4. Factors contributing to the circulation biases

This section examines in more detail reasons for the circulation biases documented in the previous section. Section 4.1 investigates this issue from a process-level perspective, especially exploring the role of differences in the representation of cold pools in the various model configurations. Section 4.2 investigates the role of model resolution versus differences in model physics across the simulations.

4.1. *Process analysis*

To explain the mechanisms underlying the differences in the breeze front propagation documented in Fig. 5, we start by considering the simulations without convective parameterisation (UCLA04, COSMO2, COSMO11 and ICON8). Rieck et al. (2015) showed by means of sensitivity experiments performed with large-eddy simulations that the presence of convection leads to an acceleration of the breeze front. This acceleration can be recognised in Fig. 5 with the UCLA04, COSMO2, COSMO11 and ICON8 curves displaying a two-phase propagation. In the first phase, e.g. from 0 to about 8 h in UCLA04, the sea breeze builds up and slowly accelerates. In the second phase (after 8 h in UCLA04) the propagation is significantly faster with a mean speed of 7.5 m s^{-1} compared to 1.5 m s^{-1} during the first four simulation hours. It follows that differences in the collision time among the simulations may result from differences in the time the breeze front begins to accelerate and/or from differences in the propagation speed after the breeze front has accelerated. Visual inspection of Fig. 5 clearly reveals that the time at which the breeze front begins to accelerate constitutes the primary source of differences among the simulations.

This visual assertion can be verified by quantifying both the time at which the breeze front begins to accelerate, denoted by T_{acc}, and the propagation speed of the breeze front. The propagation speed V is computed from the slope of a regression line fitted to the curves on Fig. 5 between $T_{col} - 1$ and $T_{col} - 4$. The derived regression lines fit very well the simulation curves during the second phase of the propagation, whereas the curves diverge from the regression lines during the first phase. The time at which the curves begin to diverge, determined as the time when the difference in the breeze front position is more than 5 km between regression line and simulation results, gives T_{acc}. As the pressure gradient inherently drives the breeze front propagation, T_{acc} can alternatively be computed by finding the time the horizontal pressure gradient reaches its maximum absolute value. The so obtained values are in the range of the ones listed in Table 1, with maximum difference of 0.5 h.

A delayed T_{col} primarily reflects a delayed T_{acc} as the variability in T_{acc} tends to be larger than the variability in V (see Table 1). In COSMO11 and ICON8 the two breeze fronts cannot collide after 14.5 h like in UCLA04 given that the breeze fronts only begin to accelerate after circa 13 h. COSMO2 depicts a larger V than UCLA04 but still exhibits a later collision than UCLA04, confirming the primary role of T_{acc}.

What causes a delayed T_{acc} in COSMO2, COSMO11 and ICON8? Rieck et al. (2015) isolated cold pools as a factor controlling the propagation of the breeze front once convection starts. The formation of cold pools by precipitation evaporation and melting of frozen hydrometeors leads to a cooling of the boundary layer air right behind the front, enhancing the temperature gradient across the front. The change in temperature gradient leads to a corresponding change in pressure gradient, which accelerates the propagation of the front. To investigate potential differences in cold pools among the simulations, Figure 6a displays the anomaly of virtual potential temperature θ_v along the x-direction, at a height of 50 m, a time of 12 h, and

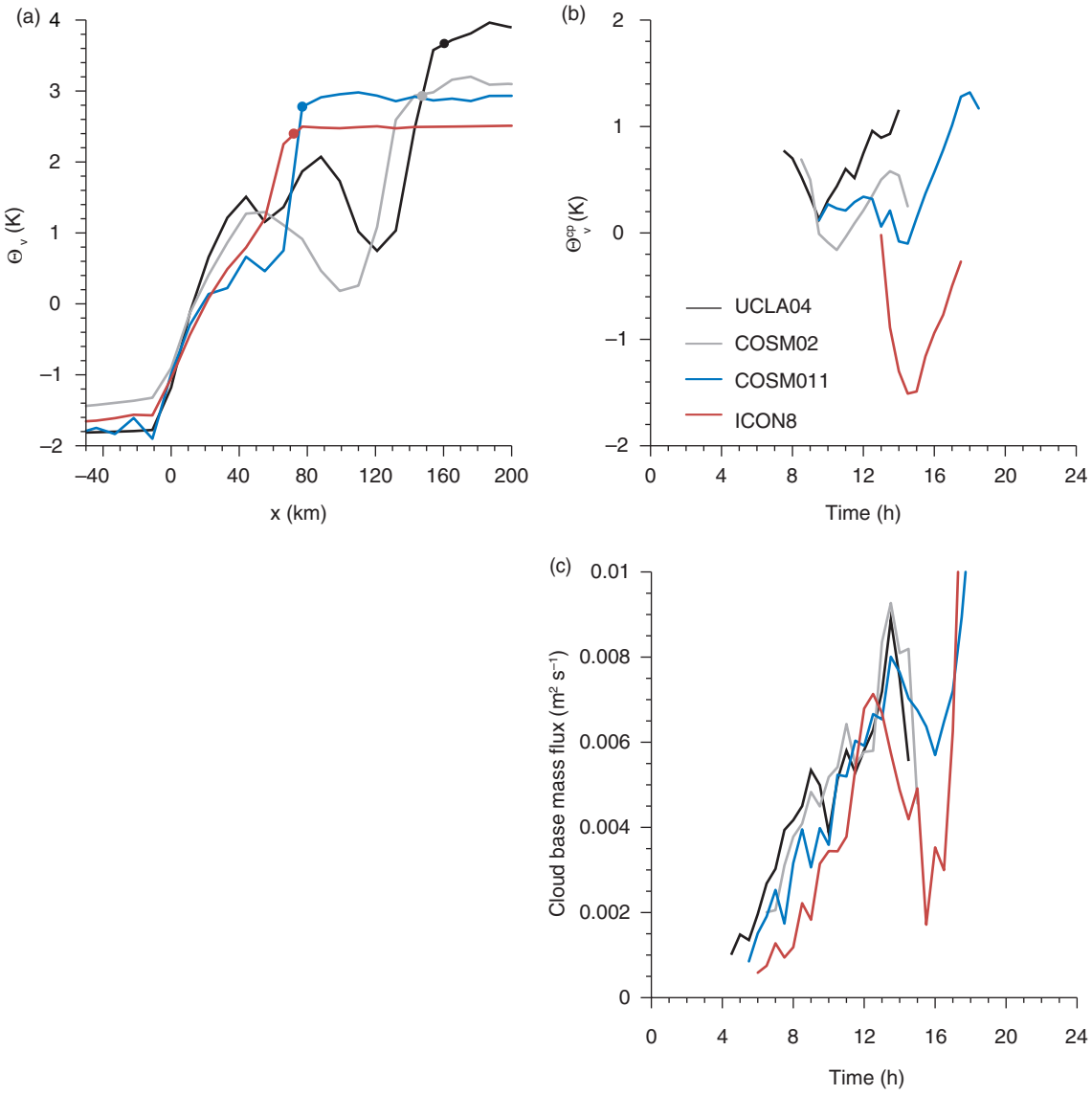

Fig. 6. Time series of (a) θ_v (K) at 50 m height and 12 h and (b) θ_v^{cp}(K), see text for details. Panel (c) shows the time series of the cloud base mass flux ($m^2\ s^{-1}$). Simulations are UCLA04 (black), COSMO2 (grey), COSMO11 (blue) and ICON8 (red). All data were coarse-grained onto the COSMO11 grid.

averaged in y-direction. The location of the breeze front at the chosen time of 12 h is marked by a dot. The existence of a cold pool can be recognised in UCLA04 by the local minimum in θ_v existing around 120 km closely behind the front position. Such a local minimum is designated for simplicity by θ_v^{cp}. θ_v^{cp} can be recognised in COSMO2; it is weak in COSMO11 and at best an inflection in ICON8. The differences in θ_v^{cp} are in agreement with the varying positions of the front at 12 h in the simulations.

The full time series of θ_v^{cp} is shown in Fig. 6b. In all the simulations, cold pools appear after precipitation started, they intensify and are then advected with the flow. This last phase generally occurs after precipitation has reached its first maximum and manifests itself by an increase in θ_v^{cp} on Fig. 6b as the surface fluxes keep on warming the land surface. Although following a similar lifecycle, the simulations reveal a very distinct timing. The intensification of cold pools is delayed in COSMO2 as compared to UCLA04 and is even more delayed in COSMO11 and ICON8 as compared to UCLA04. This delay is fully consistent with the differences in the propagation of the sea breeze found in Fig. 5 and Table 1 and is thus viewed as the main cause for such differences. Slight differences in the cold pool intensity exist among the simulations. The intensification, measured in Fig. 6b as the difference between the minimum value reached by θ_v^{cp} versus its initial value, is stronger in

COSMO2 than in UCLA04. This fits with the larger value of V in COSMO2 as compared to UCLA04 (see Table 1). Likewise COSMO11 depicts a weaker intensification and a smaller V. ICON8 depicts the strongest intensification although V is slower than in UCLA04 and COSMO2. One reason for this discrepancy may be that the maximum cooling due to the cold pools is located about 30 km behind the front in COSMO2 and UCLA04, whereas it is located around 80 km behind the front in ICON8. In any case and as mentioned earlier, such subtle differences in the intensity of cold pools and in V are not sufficient to overcome the timing differences.

An alternate hypothesis for the differences in the breeze front propagation across the simulations is that such differences arise from differences in the dynamical effect of clouds on the breeze (Rieck et al., 2015). Clouds evacuate mass (air) from the planetary boundary layer ahead of the front to deposit it on the back-side of it. This leads to a localised change in pressure gradient and accelerates the breeze front. The strength of this effect can be quantified by the flux of mass through cloud base, which is formally computed as the updraft size (from data averaged in y-direction) multiplied by the mean updraft vertical velocity (at cloud base). The updraft is defined as points where the vertical velocity is larger than 0.05 m s^{-1}. The resulting time series of the so computed cloud base mass flux is depicted in Fig. 6c.

Consideration of the various curves indicates that the relationship between the cloud base mass flux and T_{col} or T_{acc} is less clear than in Fig. 6b. For instance, the COSMO2 and COSMO11 curves display a similar timing despite the previously noted differences in T_{acc}. Only ICON8 shows a clear time lag in the time series of the cloud base mass flux during the first 12 simulation hours. It thus may be concluded that the differences seen in the sea breeze propagation in Fig. 5 among the simulations with explicit convection primarily result from differences in the appearance time of cold pools. The results bear some similarities with the findings of Weisman et al. (1997). They showed that differences in the representation of a squall line across grid spacings from 1 to 12 km relate to a delayed strengthening of the convective cold pool at coarser resolution.

Turning on the convection scheme as in COSMO11p and ICON8p leads to differences in the propagation of the breeze front as compared to UCLA04 due to differences both in the time the breeze front begins to accelerate T_{acc} and in the propagation speed V (see Fig. 5 and Table 1). In the morning, convection develops more rapidly than the sea breeze. The first breeze event mainly reveals the characteristics of a circulation directly triggered by convection rather than resulting from a convective circulation overlaying a sea breeze as found in UCLA04 or during the second breeze event (see Fig. 4). This early triggering totally disrupts the timing of the sea breeze. During the second breeze event the propagation speed attains 13.8 m s^{-1} in COSMO11p, which is much faster than in ICON8p (7.6 m s^{-1}) or UCLA04 (7.5 m s^{-1}). Figure 7 shows the temperature tendency due to the convection scheme for COSMO11p and ICON8p to shed some light on these different propagation speeds. ICON8p exhibits a more distinct mid-level heating maximum, in agreement with the different cloud population and circulation characteristics already noted in Fig. 4e and 4f and section 3. Also visible in Fig. 7 is a stronger surface cooling in COSMO11p than in ICON8p. The mean surface cooling amounts to 1 K h^{-1} in COSMO11p and 0.8 K h^{-1} in ICON8p with hourly maximum values around 8 K h^{-1} in COSMO11p but only 4 K h^{-1} in ICON8p. A stronger surface cooling enhances the temperature gradient across the breeze front and could explain the faster propagation speed V in COSMO11p as compared to ICON8p.

4.2. *Model resolution versus model physics*

Section 4.1 isolated specific processes related to convection affecting the propagation of the sea breeze in the various simulations. The biases in COSMO11p and ICON8p can be directly assigned to the specific design of the convection scheme. This is not the case for the explicit experiments. A delayed onset of cold pools may result here from a delayed onset of convection due to a too coarse grid spacing or from differences in physical parameterisations.

Figure 8a and 8b investigates the role of resolution and parameterisation choices, respectively. The results are summarised in terms of the time it takes for the front to

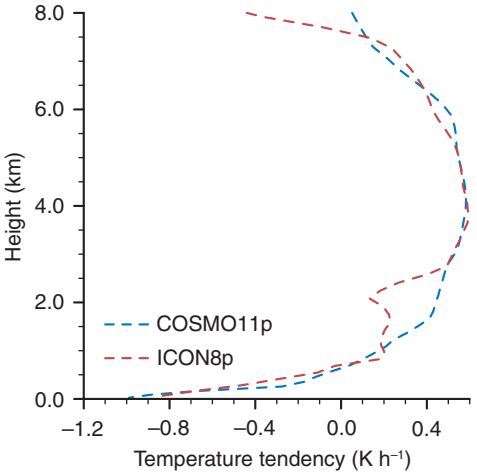

Fig. 7. Mean profile of the temperature tendency due to the convection scheme in COSMO11p and ICON8p. The time average is performed from the beginning of the simulation up to 2 h after the breeze fronts collide.

reach $x = 22$ km (T_{22}) and to collide (T_{col}). The times are expressed as differences to a control simulation, being UCLA04 for sensitivity tests performed with the UCLA-LES and COSMO2 for sensitivity tests performed with the COSMO model. A distance of 22 km is chosen because this distance is covered before convection begins to alter the propagation of the front (see Fig. 5).

Independently of the chosen model, T_{22} is not affected by the chosen grid spacing (see Fig. 8a). In contrast, a coarser resolution yields a systematic delay in T_{col} except for the UCLA-LES version with 3.2 km grid spacing. The results are robust and independent of the chosen model. A coarser resolution leads to a delayed development of convection and hence a delayed formation and intensification of cold pools. Moreover the congruent location of clouds, precipitation and the breeze front is more difficult to maintain due to the coarser resolution. Clouds and precipitation are at times located ahead of the front, which can oppose the propagation of the front.

Changing specific parameterisations at convection-permitting resolution (COSMO2) leads to timing differences of maximum 1 h (see Fig. 8b). On the one hand, the impact is weaker than the impact obtained by changing the model grid spacing. On the other hand it is in the order of magnitude of the differences obtained between UCLA04 and COSMO2 (see Tab. 1). Replacing the default turbulence scheme by the Smagorinsky scheme (see experiment TURB in Fig. 8b) delays the propagation of the breeze front. The timing differences are larger for T_{col} than for T_{22}. The two turbulence schemes simulate different vertical profiles of mixing in the planetary boundary layer, which is a known factor affecting the intensity and extent of sea breezes (Garrat et al., 1995; Finkele, 1998). The Smagorinsky scheme produces more diffusion than other turbulence schemes, implying a dilution of the pressure gradient across the breeze front and a slower propagation speed. The growth of the planetary boundary layer is also slower in TURB than in COSMO2. The slower growth yields a delayed onset of convection, a delayed acceleration of the breeze front due to convection and hence an even more delayed collision of the breeze front. Altering the representation of convection, either by including a parameterisation for shallow convection (see experiment SCU in Fig. 8b) or by switching the one-moment microphysical scheme to a two-moment scheme (see experiment MICRO in Fig. 8b), affects T_{col} in agreement with the importance of convection and cold pools for the propagation of the breeze front. Turning on shallow convection allows a slightly earlier triggering and development of convection resulting in a slightly earlier T_{col}. The impact is nevertheless weak due to the chosen initial profile and the resulting fast transition. The replacement of the one-moment by a two-moment microphysical scheme leads to a faster propagation of the breeze front by modifying the rain evaporation. The more flexible formulation of the droplet size distribution in the two-moment microphysical scheme enables the formation of smaller rain droplets which can evaporate more easily. This is supported by an analysis of the time series of θ_v^{cp}. The latter reveals a stronger cooling in MICRO than in COSMO2 (not shown). The gain in T_{col} is 0.5 h in MICRO

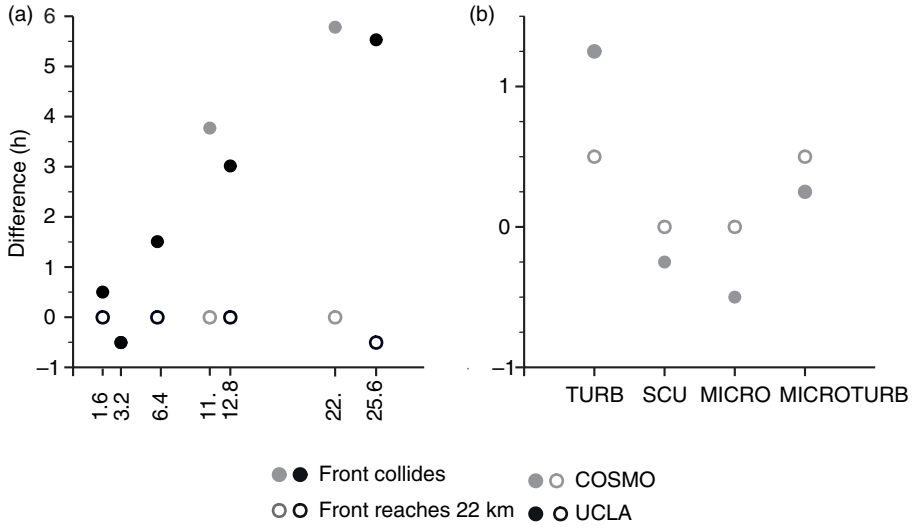

Fig. 8. Difference in time (h) it takes for the breeze front to reach 22 km (T_{22}, open circles) or to collide (T_{col}, full circles) for pair of simulations. Panel (a) investigates resolution effect for simulations run with the UCLA-LES (black points) at 1.6, 3.2, 6.4, 12.8 and 25.6 km as compared to UCLA04 as well as with COSMO (grey points) at 11 and 22 km resolutions as compared to COSMO2. Panel (b) investigates effects of parameterisation choices in COSMO2: TURB for changing the turbulence scheme, SCU for shallow convection parameterisation turned on and MICRO for changing the microphysical scheme.

and 1 h when the two-moment microphysical scheme is combined with the Smagorinsky scheme (see experiment MICROTURB in Fig. 8b).

Figure 8 also indirectly confirms that biases in the representation of convection primarily affect the propagation of the breeze front. Except for the TURB simulation, none of the sensitivity experiments of Fig. 8 is able to affect T_{22}, although they do affect T_{col} through their control on the convective properties.

5. Discussion

To explore the extent to which the lessons drawn from the control case can be generalised, Fig. 9a shows a scatterplot of the time precipitation exceeds 2 mm day^{-1} versus T_{col} for a set of five experiments per model design. The five experiments distinguish themselves by the prescribed values of sensible and latent heat fluxes over land. The fluxes are either halved or doubled, but only one of the two fluxes is changed at a time. Doubling or halving the flux values over the land section of the domain has two effects. First it modifies the buoyancy difference between the land and ocean, thus affecting the characteristics of the sea breeze (e.g. Antonelli and Rotunno, 2007). Second it can directly affect the convective development and as such the impact of convection on the breeze front propagation (Rieck et al., 2015). The choice of a threshold of 2 mm day^{-1} is motivated by the results of sections 3 and 4 which have shown that differences in the onset time of cold pools primarily explain differences in T_{col} among the experiments using explicit convection. This is not true for the experiments with parameterised convection where the too early triggering of convection and differences in the intensity of convection are expected to blur the picture. As a relationship between cold pool formation and precipitation may vary with microphysics (see 4.2), a precipitation threshold is a less accurate measure than T_{acc} or especially θ_v^{cp}. It is nevertheless an easy quantity to compute. A threshold of 2 mm day^{-1} seems to give the best results.

A delay in the time precipitation exceeds 2 mm day^{-1}, either due to a change in the chosen values of the surface fluxes or in model design in the simulations using explicit convection, yields a corresponding delay in T_{col}. All the simulations using explicit convection tend to align along a line with a slope of unity in Fig. 9a. The simulations with parameterised convection are not able to reproduce such a relationship, which is not surprising given the results of sections 3 and 4. The circulation in ICON8p induced by the morning precipitation event never projects at the surface yielding a very late T_{col} as compared to the timing of the convective development. The low-level circulation is strong enough in COSMO11p to allow a significant propagation of the breeze front in the morning hours. The open blue circles in Fig. 9a refer to this first breeze event, even though the opposing breeze fronts do not always collide.

Closer inspection of Fig. 9a reveals some subtle differences among the simulation groups. The COSMO2 and especially COSMO11p points lie below the regression line. If one assumes that a threshold of 2 mm day^{-1} is a good measure for the onset time of cold pool formation, the location of COSMO2 and COSMO11p relative to the regression line can be interpreted as a sign for stronger cold pools and hence faster V in COSMO2 and COSMO11p as compared to UCLA04. In contrast the COSMO11 points

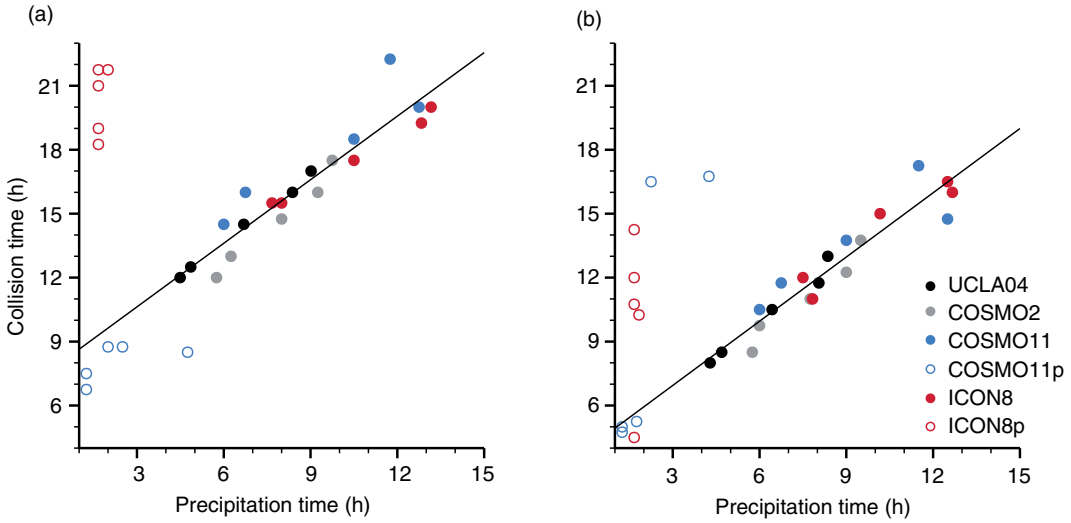

Fig. 9. Scatterplot of breeze front collision time T_{col} (h) versus time precipitation exceeds 2 mm day^{-1} for simulations with various values of sensible or latent heat fluxes over land. Simulations in (a) are integrated over the full domain of 819.2 km by 404 km; simulations in (b) utilise a domain size of 409.6 km by 404 km.

lie above the regression line, indicative of a slower V. All in all these differences tend to confirm the results of Table 1 based on the control case.

Figure 9b displays the same set of five experiments per model design but integrated over a domain of 409.6 km in x-direction instead of 819.2 km. Both ocean and land stripes are halved. Reducing the horizontal scale of the surface heterogeneity alters the sea breeze characteristics (e.g. Dalu and Pielke, 1989) and the resulting precipitation amounts (e.g. Lynn et al., 1998; Robinson et al., 2011). The smaller domain size obviously leads to shorter T_{col} in Fig. 9b but does not otherwise alter our findings.

Figure 10 shows time series of precipitation and of the front location for the stable case. The stable case sets a temperature decrease of 5.5 K per km up to 9 km, instead of 6.6 K per km as in the control case (see section 2.2 and Fig. 1). The main motivation in choosing such a gradient is to prevent the convection schemes of COSMO11p and ICON8p to trigger convection before the sea breeze can develop. As a sides effect, the use of a more stable profile implies shallower clouds and weaker precipitation amounts (see Fig. 3a and 10a). This weakens the impact of convection on the sea breeze characteristics. Comparison of Fig. 5 and 10b indeed reveals a slower propagation in all the simulations. Part of this slow-down arises from the direct effect of stability on the propagation speed, an effect also visible in dry simulations (Crosman and Horel, 2012; Antonelli and Rotunno, 2007).

Preventing convection getting in the way of the sea breeze leads to a strong improvement in the representation of the propagation of the sea breeze in COSMO11p and ICON8p. The two simulations now display only one breeze event and the differences to UCLA04 are similar or smaller than the differences between UCLA04 and COSMO11 or between UCLA04 and ICON8. Noteworthy are the two ICON simulations, where turning off the convection scheme leads to a degradation of the propagation of the sea breeze. Like in the control case, the propagation is faster in COSMO11p than in ICON8p. Despite the early formation of deep convective clouds and convective precipitation in ICON8p the convective circulation is not able to strongly affect the sea breeze as compared to COSMO11p. As found in section 4, differences in the convective heating profiles and especially a very strong rain evaporation in COSMO11p contribute to those discrepancies.

The simulations with explicit convection exhibit a similar behaviour as in the control case. A delayed development of convection and precipitation yields a corresponding delay in the acceleration of the breeze front through a delayed formation and intensification of cold pools and hence a delayed collision, see Fig. 10a and 10b. The comparison of the stable (Fig. 10) and control cases (Fig. 5) reveals one difference in the ordering of T_{col}. The collision occurs at a later time in ICON8 than in COSMO11 in the stable case. This difference is nevertheless in full agreement with the displayed precipitation time series. The precipitation curve of ICON8 is characterised by a time lag of more than 2 h between 14 h and 18 h with respect to COSMO11 and the front only begins to accelerate shortly before the collision.

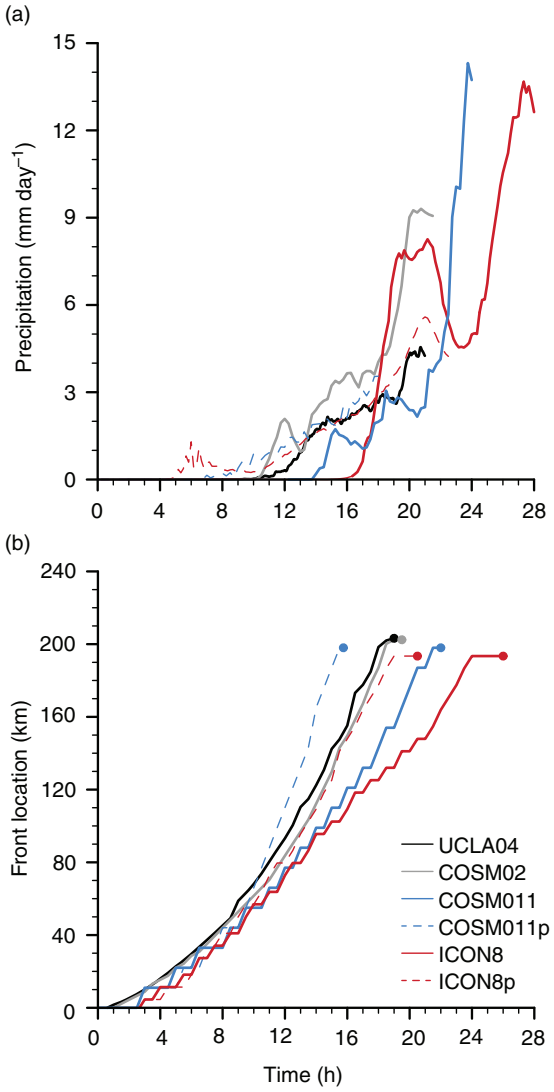

Fig. 10. As Fig. 3a and 5 but for the stable profile (see Fig. 1).

Although based on idealised simulations, the results should be applicable to realistic configurations. Sea breezes are expected to develop following the diurnal cycle of insolation, typically starting around 6 am in the tropics, which is also the time convection can start to be triggered and precipitation being produced in climate models (see e.g. Fig. 7 in Hohenegger and Stevens 2013). By correcting the problem of an early triggering of convection over land in the IFS, Bechtold et al. (2013) documented a more realistic propagation of the monsoon over the African

continent. This is consistent with the results of Marsham et al. (2013) who, by comparing coarse-resolution simulations with and without convection scheme, have shown that a correct representation of the African monsoon by a convective parameterisation requires a correct timing of precipitation and a parameterisation for cold pools. An explicit representation of cold pools seems not per se necessary in our case as neither COSMO11p nor ICON8p include such a formulation. However, a correct representation of rain evaporation appears crucial. By altering the diurnal cycle of convection in climate models several studies (e.g. Wang et al., 2007; Sato et al., 2009; Hohenegger and Stevens, 2013) have also reported improvements in the representation of precipitation over island regions without having quantified in detail the effects of their modifications on the sea breeze characteristics. The use of diagnostics as introduced in sections 3 and 4, especially Table 1, Fig. 6 and Fig. 9, could help isolating shortcomings in the representation of the coupling between convection and thermally induced circulation in realistic configurations and across model set-ups.

6. Conclusions

This study investigated the coupling between convection and a sea breeze at three main resolutions: large-eddy resolution where convection is fully explicit, convection-permitting resolution where convection is partly explicit and coarse resolution where convection is parameterised. The simulations were performed with three models that have been designed to work on such scales: the UCLA-LES run at 400 m for the large-eddy simulations, the COSMO model run at 2.2 km for the convection-permitting experiments and the COSMO and ICON models run at 11 km and 8.5 km for the coarse-resolution simulations. Further sensitivity experiments have been performed by systematically varying the grid spacing and by changing physical parameterisations.

Biases in the representation of convection are found to significantly alter the characteristics of the sea breeze despite the use of prescribed surface fluxes. The time the two opposing breeze fronts triggered by the land-sea discontinuity collide in the centre of the land patch can vary by as much as 10 h among the simulations. The convection-permitting and coarse-resolution simulations integrated without convection scheme exhibit both a too late triggering of convection and a too late collision of the opposing breeze fronts as compared to the large-eddy simulations. Turning on the convection scheme produces an early triggering of convection and two breeze events. The first breeze event mainly reflects the characteristics of a circulation directly triggered by convection rather than resulting from a convective circulation overlaying a sea breeze as found during the second breeze event or in the large-eddy simulations.

The propagation of a breeze front depends upon the buoyancy difference between land and ocean, the timing and magnitude of cloud dynamical effects as well as the timing and magnitude of cold pools (Rieck et al., 2015). The delayed collision of the breeze fronts in the experiments integrated at convection-permitting and coarser resolution without convective parameterisation primarily arises due to differences in the timing of cold pools. Coarser resolutions yield a delayed development of convection, a delayed production of precipitation, a delayed formation and intensification of cold pools, a delayed acceleration of the breeze front by the cold pools and hence a delayed collision. The use of different parameterisations, in particular boundary layer and microphysics, affects the magnitude of cold pools and the propagation speed of the breeze front but the impacts are generally too weak to overcome the resolution effect.

In the case with parameterised convection, differences in the propagation of the breeze front arise both from timing and magnitude differences in the parameterised convective processes. First and foremost the too early triggering of convection strongly disrupts the interactions between convection and the sea breeze. Second, of the two tested convection schemes, the Tiedtke (1989) scheme (used in COSMO) causes an anomalously fast propagation of the breeze front likely due to a too strong evaporation of precipitation. The second tested convection scheme (Bechtold et al., 2008, used in ICON) produces less rain evaporation and a convective circulation that is more pronounced in the middle rather than in the lower layers due to differences in the simulated cloud population. This results in a propagation speed that is almost half that of the Tiedtke (1989) scheme and more akin to the results of the large-eddy simulations. The propagation speed compares even better with the propagation speed of the large-eddy simulations than when the convection scheme is turned off.

Although neither the convection-permitting nor the coarse-resolution simulations can reproduce the large-eddy simulation results, the convection-permitting simulation represents a definite improvement over the coarse-resolution simulations. The timing, both of the precipitation and of the sea breeze, as well as the relative location of the cloud, precipitation and breeze front are improved. The main issue at convection-permitting scales remains the slightly late triggering of convection. Switching on the convection scheme at coarse resolution in general degrades the simulation. However, depending on the chosen convection scheme, preventing the convection scheme from firing too quickly can produce a sea breeze that is more akin to the large-eddy simulations.

All in all the results emphasise that, although the development of convection is strongly influenced by the presence of a sea breeze, convection also strongly affects the sea breeze characteristics. The use of the time precipitation exceeding 2 mm day^{-1} is found to be a good indicator for the time the opposing breeze fronts collide in the centre of the land patch in the various experiments. At the same time, relationships between these two timescales can reveal differences in the way convection and sea breezes couple across resolutions. Although focusing on a sea breeze, the results should be applicable to other types of thermally induced circulations (e.g. vegetation breezes) given their shared similarities. As such, the employed simulation set-up may be seen as a valuable test for investigating convection–circulation coupling in different model configurations.

7. Acknowledgements

The study was supported by the Hans Ertel Centre for Weather Research and by the Max Planck Society for the advancement of science. The Hans Ertel Centre for Weather Research is a research network of Universities, Research Institutes and the Deutscher Wetterdienst funded by the BMVBS (Federal Ministry of Transport, Building and Urban Development). The authors thank Bjorn Stevens and two reviewers for helpful comments on this manuscript.

References

Ackerman, A. S., van Zanten, M. C., Stevens, B., Savic-Jovcic, V., Bretherton, C. S. and co-authors. 2009. Large-eddy simulations of a drizzling, stratocumulus-topped marine boundary layer. *Mon. Weather Rev.* **137**, 1083–1110.

Antonelli, M. and Rotunno, R. 2007. Large-eddy simulation of the onset of the sea breeze. *J. Atmos. Sci.* **64**, 4445–4457.

Baldauf, M., Seifert, A., Förstner, J., Majewski, D., Raschendorfer, M. and co-authors. 2011. Operational convective-scale numerical weather prediction with the COSMO model: description and sensitivities. *Mon. Weather Rev.* **139**, 3887–3905.

Bechtold, P., Köhler, M., Jung, J., Doblas-Reyes, F., Leutbecher, M. and co-authors. 2008. Advances in simulating atmospheric variability with the ECMWF model: from synoptic to decadal time-scales. *Q. J. Roy. Meteorol. Soc.* **134**, 1337–1351.

Bechtold, P., Semane, N., Lopez, P., Chaboureau, J. P., Beljaars, A. and co-authors. 2013. Breakthrough in forecasting equilibrium and non-equilibrium convection. *ECMWF Newsl.* **136**, 15–23.

Benjamin, T. B. 1968. Gravity currents and related phenomena. *J. Fluid. Mech.* **31**, 209–248.

Berg, L. C. J. and Oerlemans, J. 1985. Simulation of the sea-breeze front with a model of moist convection. *Tellus* **37A**, 30–40.

Bony, S., Stevens, B., Frierson, D. M. W., Jakob, C., Kageyama, M., and co-authors. 2015. Clouds, circulation and climate sensitivity. *Nat. Geosci.* (in press).

Brockhaus, P., Lüthi, D. and Schär, C. 2008. Aspects of the diurnal cycle in a regional climate model. *Meteorol. Z.* **17**, 433–443.

Burpe, R. W. and Lahiff, L. N. 1983. Area-average rainfall variations on sea-breeze days in South Florida. *Mon. Weather Rev.* **112**, 520–534.

Cohen, C. 2002. A comparison of cumulus parameterizations in idealized sea-breeze simulations. *Mon. Weather Rev.* **130**, 2554–2571.

Crosman, E. T. and Horel, J. D. 2010. Sea and lake breezes: a review of numerical studies. *Bound.-Layer Meteor.* **137**, 1–29.

Crosman, E. T. and Horel, J. D. 2012. Idealized large-eddy simulations of sea and lake breezes: sensitivity to lake diameter, heat flux and stability. *Bound.-Layer Meteor.* **144**, 309–328.

Dai, A. G. 2006. Precipitation characteristics in eighteen coupled climate models. *J. Climate* **19**, 4605–4630.

Dalu, G. and Pielke, R. 1989. An analytical study of the sea breeze. *J. Atmos. Sci.* **46**, 1815–1825.

De Rooy, W. C., Bechtold, P., Fröhlich, K., Hohenegger, C., Jonker, H. and co-authors. 2013. Entrainment and detrainment in cumulus convection: an overview. *Q. J. Roy. Meteorol. Soc.* **139**, 1–19. DOI: 10.1002/qj.1959.

Derbyshire, S. H., Beau, I., Bechtold, P., Grandpeix, J. Y., Piriou, J. M. and co-authors. 2004. Sensitivity of moist convection to environmental humidity. *Q. J. Roy. Meteorol. Soc.* **130**, 3055–3079.

Doms, G., Förstner, J., Heise, E., Herzog, H. M., Mironov, D. and co-authors. 2011. A description of the nonhydrostatic regional COSMO model part II: physical parameterization. German Weather Service, Offenbach, Germany. Online at: http//www.cosmo-model.org/content/model/documentation/core/default.htm.

Finkele, K. 1998. Inland and offshore propagation speeds of a sea breeze from simulations and measurements. *Bound.-Layer Meteor.* **87**, 307–329.

Garcia-Carreras, L., Marsham, J. H., Parker, D. J., Bain, C. L., Milton, S. and co-authors. 2013. The impact of convective cold pool outflows on model biases in the Sahara. *Geophys. Res. Lett.* **40**, 1647–1652.

Garrat, J. R., Hess, G. D., Physick, W. L. and Bougeault, P. 1995. The atmospheric boundary layer-advances in knowledge and application. *Bound.-Layer Meteor.* **78**, 9–37.

Gill, A. E. 1980. Some simple solutions for heat-induced tropical circulation. *Q. J. Roy. Meteorol. Soc.* **106**, 447–462.

Halley, E. 1753. An historical account of the trade winds and monsoons observable in the Seas between and near the Tropicks with an attempt to assign the physical cause of the land winds. *Proc. R. Soc. London* **16**, 153–173.

Hohenegger, C., Brockhaus, P. and Schär, C. 2008. Towards climate simulations at cloud-resolving scales. *Meteorol. Z.* **17**, 383–394.

Hohenegger, C. and Stevens, B. 2013. Controls on and impacts of the diurnal cycle of deep convective precipitation. *J. Adv. Model. Earth Syst.* **5**, 801–815.

Kain, J. S., Weiss, S. J., Levit, J. J., Baldwin, M. E. and Bright, D. R. 2006. Examination of convection-allowing configurations of the WRF model for the prediction of severe convective weather: the SPC/NSSL spring program 2004. *Wea. Forecasting* **21**, 167–181.

Kuell, V. and Bott, A. 2008. A hybrid convection scheme for use in non-hydrostatic numerical weather prediction models. *Meteorol. Z.* **17**, 775–783.

Kühlein, C., Keil, C., Craig, G. C. and Gebhardt, C. 2014. The impact of downscaled initial condition perturbations on convective-scale ensemble forecasts of precipitation. *Q. J. Roy. Meteorol. Soc.* **140**, 1552–1562.

Langhans, W., Schmidli, J., Fuhrer, O., Bieri, S. and Schär, C. 2013. Long-term simulations of thermally driven flows and orographic convection at convection-parameterizing and cloud-resolving resolutions. *J. Appl. Meteor. Climatol.* **52**, 1490–1510.

Lean, H. W., Clark, P. A., Dixon, M., Robers, N. M., Fitch, A. and co-authors. 2008. Characteristics of high-resolution versions of the Met Office unified model for forecasting convection over the United Kingdom. *Mon. Weather Rev.* **136**, 3408–3424.

Lynn, B. and Khain, A. 2007. Utilization of spectral bin microphysics and bulk parameterization schemes to simulate the cloud structure and precipitation in a mesoscale rain event. *J. Geophys. Res.* **112**, DOI: 10.1029/2007JD008475.

Lynn, B. H., Stauffer, D. R., Wetzel, P. J., Tao, W.-K., Alpert, P. and co-authors. 2001. Improved simulation of Florida summer convection using the PLACE land model and a 1.5-order turbulence parameterization coupled to the Penn State-NCAR mesoscale model. *Mon. Weather Rev.* **129**, 1441–1461.

Lynn, B. H., Tao, W.-K. and Wetzel, P. 1998. IA study of landscape-generated deep moist convection. *Mon. Weather Rev.* **126**, 928–942.

Marsham, J. H., Dixon, N. S., Garcia-Carreras, L., Lister, G. M. S., Parker, D. J. and co-authors. 2013. The role of moist convection in the West African monsoon system: insights from continental-scale convection-permitting simulations. *Geophys. Res. Lett.* **40**, 1843–1849.

Mellor, G. L. and Yamada, T. 1982. Development of a turbulence closure model for geophysical fluid problems. *Rev. Geophys. Space Phys.* **20**, 851–875.

Nicholls, M. E., Pielke, R. A. and Cotton, W. R. 1991. A two-dimensional numerical investigation of the interaction between sea breezes and deep convection over the Florida Peninsula. *Mon. Weather Rev.* **119**, 298–323.

Pearson, K. J., Lister, G. M. S., Birch, C. E., Allan, R. P., Hogan, R. J. and co-authors. 2014. Modelling the diurnal cycle of tropical convection across the 'grey zone'. *Q. J. R. Meteorol. Soc.* **140**, 491–499.

Petch, J. C., Brown, A. R. and Gray, M. E. B. 2006. The impact of horizontal resolution on the simulations of convective development over land. *Q. J. R. Meteorol. Soc.* **128**, 2031–2044.

Pielke, R. A. 1974. A three dimensional numerical model of the sea breezes over south Florida. *Mon. Weather Rev.* **102**, 115–139.

Prein, A. F., Gobiet, A., Suklitsch, M., Truhetz, H., Awan, N. K. and co-authors. 2013. Added value of convection permitting seasonal simulations. *Clim. Dynamics* **41**, 2655–2677.

Raschendorfer, M. 2001. The new turbulence parameterization of LM. *COSMO Newsl.* **1**, 89–97.

Reinhardt, T. and Seifert, A. 2006. A three-category ice scheme for LMK. *COSMO Newsl.* **6**, 115–120.

Rieck, M., Hohenegger, C. and Gentine, P. 2015. The influence of moist convection on thermally induced mesoscale circulations. *Q. J. R. Meteorol. Soc.* DOI: 10.1002/qj.2532.

Rieck, M., Hohenegger, C. and van Heerwaarden, C. C. 2014. The influence of land surface heterogeneities on cloud size development. *Mon. Weather Rev.* **142**, 3830–3846.

Robinson, F. J., Patterson, M. D. and Sherwood, S. C. 2013. A numerical modeling study of the propagation of idealized sea-breeze density currents. *J. Atmos. Sci.* **70**, 653–668.

Robinson, F. J., Sherwood, S. C., Gerstle, D., Liu, C. and Kirshbaum, D. J. 2011. Exploring the land-ocean contrast in convective vigor using islands. *J. Atmos. Sci.* **68**, 602–618.

Rotunno, R. 1983. On the linear theory of the land and sea breeze. *J. Atmos. Sci.* **40**, 1999–2009.

Sato, T., Miura, H., Satoh, M., Takayabu, Y. N. and Wang, Y. 2009. Diurnal cycle of precipitation in the tropics simulated in a global cloud-resolving model. *J. Climate* **22**, 4809–4826.

Segal, M., Purdom, J. F. W., Song, J. L., Pielke, R. A. and Mahrer, Y. 1986. Evaluation of cloud shading effects on the generation and modification of mesoscale circulations. *Mon. Weather Rev.* **114**, 1201–1212.

Seifert, A. and Beheng, K. 2006. A two-moment cloud microphysics parameterization for mixed-phase clouds. Part I model description. *Meteorol. Atmos. Phys.* **92**, 45–66.

Siebesma, A., Bretherton, C., Brown, A., Chlond, A., Cuxart, J. and co-authors. 2003. A large eddy simulation intercomparison study of shallow cumulus convection. *J. Atmos. Sci.* **60**, 1201–1219.

Slingo, J., Inness, P., Neale, R., Woolnough, S. and Yang, G. Y. 2003. Scale interactions on diurnal to seasonal timescales and their relevance to model systematic errors. *Ann. Geophys.* **46**, 139–155.

Stevens, B., Moeng, C., Ackerman, A., Bretherton, C. S., Chlond, A. and co-authors. 2005. Evaluation of large-eddy simulations via observations of nocturnal marine stratocumulus. *Mon. Weather Rev.* **133**, 1443–1462.

Taylor, C. M., Birch, C. E., Parker, D. J., Dixon, D. N., Guichard, F. and co-authors. 2013. Modeling soil moisture-precipitation feedback in the Sahel: importance of spatial scale versus convective parameterization. *Geophys. Res. Lett.* **40**, 6213–6218.

Tiedtke, M. 1989. A comprehensive mass flux scheme for cumulus parameterization in large-scale models. *Mon. Weather Rev.* **117**, 1779–1800.

Van Zanten, M. C., Stevens, B., Nuijens, L., Siebesma, A. P., Ackerman, A. S. and co-authors. 2011. Controls on precipitation and cloudiness in simulations of trade-wind cumulus as observed during RICO. *J. Adv. Model. Earth Syst.* **3**, DOI: 10.1029/2011MS000056.

Wan, H., Giorgetta, M., Zängl, G., Restelli, M., Majewski, D. and co-authors. 2013. The ICON-1.2 hydrostatic atmospheric dynamical core on triangular grids – part 1 formulation and performance of the baseline version. *Geosci. Model Dev.* **6**, 735–763.

Wang, Y., Zhou, L. and Hamilton, K. 2007. Effect of convective entrainment/detrainment on the simulation of the tropical precipitation diurnal cycle. *Mon. Weather Rev.* **135**, 567–585.

Weisman, M. L., Skamarock, W. C. and Klemp, J. B. 1997. The resolution dependence of explicitly modeled convective systems. *Mon. Weather Rev.* **125**, 527–548.

Yang, Y. and Slingo, J. 2001. The diurnal cycle in the tropics. *Mon. Weather Rev.* **129**, 784–801.

Zängl, G., Reinert, D., Ripodas, P. and Baldauf, M. 2014. The ICON (ICOsahedral Non-hydrostatic) modelling framework of DWD and MPI-M: description of the non-hydrostatic dynamical core. *Q. J. Roy. Meteorol. Soc.* DOI: 10.1002/qj.2378.